J Adv Ceram

Research Article

High-temperature structural evolution and mosaic-shell formation of sinoite fibers resistant to 1700 °C

Zhiqian Liu, Xin Long, Qiansi Zhang, Zhangbocheng Tang, Bing Wang✉, Changwei Shao✉

Cite this article: Liu Z, Long X, Zhang Q, et al. *J Adv Ceram* 2026, **15**(4): 9221265. https://doi.org/10.26599/JAC.2026.9221265

ABSTRACT: Low-dielectric continuous ceramic fibers with thermal and load-bearing functions serve as critical raw materials for accident-tolerant ceramic composites in aerospace shuttles. Silicon oxynitride ceramics exhibit a temperature resistance exceeding 1700 °C, which holds potential applications in extreme thermal protection materials. According to the attractive potential properties of silicon oxynitride ceramics, this study develops continuous silicon oxynitride (sinoite) fibers with a near-stoichiometric Si_2N_2O ratio and a tensile strength of 1.53 GPa via the precursor conversion method. The research investigates the relationships between composition and microstructure, demonstrating mechanical properties and high-temperature evolution. Sinoite fibers retain 65% of their strength at 1600 °C in a nitrogen atmosphere. After 1700 °C treatment, Si_2N_2O crystallization formed on the surface layer, elucidating the mosaic-shell formation mechanism in high-temperature evolution. Despite extremely low porosity, the strength retention rate remained up to 51%. To the best of our knowledge, this study provides a novel sinoite fiber with outstanding heat resistance up to 1700 °C for the first time. The sinoite fibers exhibit excellent properties compared with alumina, silicon nitride, and mullite fibers, offering promising reinforcement for thermal protection systems and electromagnetic components served in extreme environments.

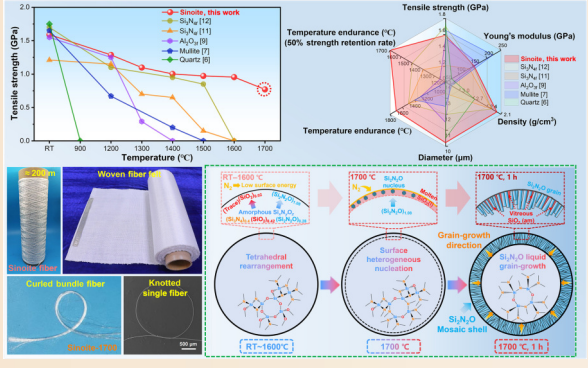

KEYWORDS: sinoite fibers; structural and property evolution; high-temperature resistance; grain-growth mechanism

1 Introduction

With the rapid advancement of advanced aerospace equipment, there is an urgent demand for high-performance-integrated structural and functional materials in extreme thermal protection components for new-generation aircraft. Oxide and nitride ceramic fibers, which combine thermal protection and load-bearing capabilities, serve as the key reinforcing phases in electromagnetic wave-transparent ceramic composites [1–3]. Currently, the reinforcing fibers used in high-temperature-resistant ceramic matrix composites are represented by alumina fibers among oxides, as well as nitride fibers such as silicon nitride fibers [4,5]. Alumina fibers exhibit excellent mechanical and dielectric properties at room temperature with relatively low cost [6,7]. However, alumina fibers exhibit rapid grain growth and crystallization of α-Al_2O_3 and γ-Al_2O_3 phases above 1400 °C [8,9]. Silicon nitride fibers exhibit superior mechanical properties, outstanding dielectric performance, and excellent high-temperature resistance, meeting operational requirements in short-term inert environments up to 1500 °C [10,11]. After treating amorphous silicon nitride fibers at 1500 °C for 1 h, the fiber strength decreased from 1.55 to 0.55 GPa, with distinct α-Si_3N_4 and β-Si_3N_4 phases appearing at 1500 °C [12]. Some researchers also observed that after treating Si_3N_{4f} at 1400 °C in a nitrogen atmosphere, its strength decreased from 1.1 to 0.44 GPa, further dropping to 0.13 GPa at 1450 °C [3]. Oxygen-containing silicon nitride fibers, or SiNO fibers, were reported in limited quantities during the last century due to their superior high-temperature resistance [13,14]. Researchers employed a high-temperature gas–solid process using NH_3 to nitride SiO_2, yielding extremely fine Si–N–(O) fibers. At 1500 °C, the surface layer crystallized into α-Si_3N_4, resulting in a decrease in strength [15]. It is observed that oxygen-containing silicon nitride fibers crystallized at 1000 °C, forming α-Si_3N_4 at 1400 °C with accompanying strength reduction through nitridation of polycarbosilane. [14]. Evidently, the significant degradation of tensile strength in silicon nitride or oxygen-containing silicon nitride fibers at high temperatures is closely related to excessive grain growth [16]. This directly impacts the temperature resistance of oxide and nitride ceramic fibers, posing a challenge for the application of ceramic fiber-reinforced

Science and Technology on Advanced Ceramic Fibers and Composites Laboratory, College of Aerospace Science and Engineering, National University of Defense Technology, Changsha 410073, China.

✉ Corresponding authors. E-mail: B. Wang, bingwang@nudt.edu.cn; C. Shao, chwshao@126.com

Received: November 8, 2025; Revised: December 17, 2025; Accepted: February 13, 2026

© The Author(s) 2026. This is an open access article under the terms of the Creative Commons Attribution 4.0 International License (CC BY 4.0, http://creativecommons.org/licenses/by/4.0/).

ceramic matrix composites in extremely high-temperature environments.

Silicon oxynitride (sinoite) ceramics originate from silicon oxynitride discovered in meteorites. As the only stable structure between silicon dioxide and silicon nitride, it possesses the combined properties of silicon dioxide and silicon nitride while maintaining excellent thermodynamic stability [17,18]. Its stable structure confers excellent high-temperature resistance, thermal shock resistance, favorable mechanical properties, and a low thermal expansion coefficient [19,20]. Some researchers prepared transparent Si_3N_4–SiO_2 ceramics capable of withstanding 1800 °C through a two-step sintering process. These materials exhibited excellent flexural strength (δ = 210–236 MPa) and suitable dielectric properties (ε < 4.8, tanδ < 0.0044) [21]. Dense silicon oxynitride ceramics have been prepared by hot-pressing oxidized amorphous Si_3N_4 powder at 1700 °C [22]. These ceramics exhibited a flexural strength of 311±14.9 MPa at 1400 °C and a loss tangent value below 5×10^{-3}. Therefore, silicon oxynitride ceramics exhibit outstanding temperature resistance, a low dielectric constant, and low dielectric loss. The Si_2N_2O crystals formed at high temperature are composed of SiN_3O silicon tetrahedra connected by oxygen bridges [17,22]. Their theoretical decomposition temperature is approximately 1900 °C, with a temperature resistance exceeding 1700 °C in an inert atmosphere [23]. Silicon oxynitride ceramics have thus become a hotspot in high-temperature ceramic composite research both domestically and internationally. Given the superior properties of Si_3N_4 ceramics, ceramic fibers exhibiting high crystallization temperatures and forming Si_2N_2O crystals should possess enhanced temperature resistance. To the best of our knowledge, few studies have focused on continuous sinoite fibers with stable structures and outstanding high-temperature resistance. Therefore, developing continuous sinoite fibers holds significant importance for advancing the temperature resistance limits of both oxide and nitride fibers.

In this work, we have successfully developed continuous sinoite fibers with near-stoichiometric composition for the first time. This breakthrough addresses the common issues of low crystallization temperatures and excessive grain growth in conventional nitride and oxide fibers, enabling sinoite fibers to withstand temperatures up to 1700 °C. After 1 h of treatment at 1700 °C, sinoite fibrous crystals grew along the fiber diameter, revealing the grain-growth mechanism of the mosaic-shell structure at high temperatures. Molecular dynamics simulations indicate that sinoite fibers with near-stoichiometric Si_2N_2O ratios are more conducive to maintaining structural and thermodynamic stability, facilitating Si_2N_2O crystallization at elevated temperatures.

2 Materials and methods

2.1 Experimental

Silicon oxynitride ceramics exhibit exceptional high-temperature resistance due to the crystallization of Si_2N_2O at elevated temperatures, offering significant advantages in practical applications. Leveraging the intrinsic properties of silicon oxynitride ceramics, this study has successfully developed continuous sinoite fibers. The sinoite fibers were fabricated using the t-BuOSZ precursor reported previously by our group [24]. The spinnable t-BuOSZ precursor was synthesized with the ammonolysis polymerization of the monomer t-BuOSiCl_2 under optimized conditions. The green fibers were obtained by melt-spinning of the t-BuOSZ polymer at 210 °C and then subjected to curing at 150 °C under air. To minimize the carbon content, the cured fibers were pyrolyzed in ammonia/nitrogen (v/v = 1 : 1) with a total gas flow of 5 L/min up to 1000 °C. The fibers were further treated at temperatures up to 1400 °C under a 2 L/min flow of high-purity nitrogen atmosphere. The heating rate for each stage was 5 °C/min. After cooling to room temperature, the sinoite fibers were obtained, and their fundamental high-temperature composition, structure, and properties were investigated.

As shown in Fig. S1 in the Electronic Supplementary Material (ESM), the novel developed continuous sinoite fiber can reach a length of approximately 200 m and possesses suitable woven fiber felt. The elemental percentages of silicon, nitrogen, oxygen, and carbon in the fiber are 51.07, 30.32, 16.82, and 0.12 wt%, respectively, with a stoichiometric ratio approximating the composition of Si_2N_2O. As shown in Table 1, the fiber exhibits an average diameter of 10.23 μm, with a tensile strength of 1.53 GPa, Young's modulus of 151 GPa, density of 2.29 g/cm^3, dielectric constant of 2.771, and dielectric loss of 1.11×10^{-4}. Thus, the novel sinoite fiber exhibits light-weight, high-strength, and low-dielectric properties, with its relatively high resistivity correlating to extremely low carbon content.

The carbon content was determined using an EMIA-320V carbon–sulfur analyzer; oxygen and nitrogen contents were measured with an EMGA-830 oxygen–nitrogen analyzer; silicon content was measured using Axios X-ray fluorescence spectroscopy. The fiber density was determined based on Archimedes' principle using a Mettler Toledo XPE 205 analytical balance via the ethanol displacement method. The mechanical properties of the fiber were tested using a Testometrix Micro 350 tensile strength tester to measure the tensile strength and modulus of individual fiber filament samples. The sample gauge length was 25 mm, and the tensile rate of the grips was 5 mm/min. 24 samples were tested per fiber group, and the data dispersion values were calculated. The complex permittivity and tangent of the loss angle of the fiber were measured using the rectangular resonant cavity perturbation method. The values at 9656 MHz were obtained using the PR1030V02N14 complex permittivity measurement system for rectangular cavities.

2.2 Characterizations

The morphology of the samples was analyzed using a MIRA3 LMH scanning electron microscope (Tescan) at a scanning voltage of 10 kV. Surface roughness was measured with a Bruker Dimension Icon scanning probe atomic force microscope (AFM). Fiber cross-sections were prepared by sectioning through the center using a focused ion beam (FIB) system, specifically the

Table 1 Basic physical and chemical properties and performance parameters of novel sinoite fibers

Chemical composition (wt%)	Si	51.07
	N	30.32
	O	16.82
	C	0.12
Stoichiometric ratio		$Si_{1.82}N_{2.16}O_{1.05}$
Tensile strength (GPa)		1.53±0.39
Young's modulus (GPa)		151±12
Density (g/cm^3)		2.29
Diameter (μm)		10.23±1.24
Dielectric constant		2.771
Dielectric loss		1.11×10^{-4}
Electrical resistivity (Ω·m)		4.32×10^{12}

Tescan AMBER GMH dual-beam electron microscope. Further analysis of the microstructure and composition of the cross-section samples was conducted using a JEM-F200 transmission electron microscope (TEM; JEOL) equipped with an Ultim Max 80 energy dispersive spectrometer (EDS; Oxford Instruments) and selected area electron diffraction (SAED) micrographs. The accelerated electron energy was 300 keV, with a point resolution of 0.06 nm. The sections were also observed using a ThermoFisher Spectra 300 aberration-corrected transmission electron microscope, with electron energy loss spectroscopy (EELS) analysis performed using a 1066 GIF spectrometer (Gatan). Elemental bonding states on the fiber surface and interior were analyzed using a ESCALAB 250 X-ray photoelectron spectroscopy (XPS) spectrometer (Thermo Fisher). A Bruker D8 ADVANCED X-ray diffractometer (XRD) was employed to analyze the crystal structure of the samples. Testing conditions were as follows: Cu Kα radiation, tube voltage 40 kV, tube current 40 mA, λ = 1.5406 Å, 2θ = 10°–90°. Spectral-grade KBr powder was dried and pressed into pellets for analysis using a Nicolet-360 (Thermo Fisher) Fourier transform infrared (FT-IR) spectrometer, which scanned the wavenumber range from 500 to 4000 cm^{-1}. Solid-state ^{29}Si magic-angle spinning nuclear magnetic resonance (^{29}Si MAS NMR) was employed to characterize the silicon tetrahedral structure. Experiments were conducted on a JNM-ECZ600R (JEOL) spectrometer operating at 119.2 MHz. Data acquisition utilized a single-pulse method with a sample rotation speed of 12 kHz, relaxation time of 5 s, and a sampling duration of 12 h. Surface analysis, depth profiling, and three-dimensional atomic imaging of the samples were performed using time-of-flight secondary ion mass spectrometry (TOF-SIMS) on IONTOF5-100 (IONTOF). Etching was conducted in Cs^+ negative ion mode at a rate of 0.84 nm/s. Wide-angle X-ray scattering (WAXS) and small-angle X-ray scattering (SAXS) characterized the crystalline orientation and microporous distribution of the samples, yielding one-dimensional and two-dimensional (2D) distributions and images, respectively. WAXS measurements were performed using a Xenocs Xeuss 3.0 UHR diffractometer, while SAXS measurements were conducted at the BL16B1 synchrotron radiation beamline of the Shanghai Synchrotron Radiation Facility, equipped with a Pilatus 2M detector.

Among these, the grain sizes corresponding to different crystal planes in WAXS/XRD are calculated using the Scherrer equation [25], as expressed by Eq. (1):

$$D = \frac{K\lambda}{\beta\cos\theta} \tag{1}$$

where D is the grain size perpendicular to the (hkl) plane; K is the Scherrer constant, taken as 0.89 when β is the full width at half maximum (FWHM); λ is the incident X-ray wavelength, which is 1.54056 Å for Cu Kα; and θ is the Bragg diffraction angle.

The interplanar spacing d in WAXS is obtained using the Bragg equation (Eq. (2)):

$$d = \frac{n\lambda}{2\sin\theta} = \frac{2\pi}{q} \tag{2}$$

where n is the diffraction order, and q is the scattering vector.

The polar azimuth angle (χ) in WAXS 2D images yields the azimuthal intensity distribution curve $I(\chi)$ after integration. The expression for Herman's orientation factor ($f_{Hermans}$) [26], is given by Eq. (3):

$$f_{Hermans} = \frac{3\int_0^{\frac{\pi}{2}} I(\chi)\cos^2\chi\sin\chi d\chi}{2\int_0^{\frac{\pi}{2}} I(\chi)\sin\chi d\chi} - \frac{1}{2} \tag{3}$$

The distance distribution function $P(r)$ in SAXS is obtained by applying a Fourier transform to the Debye–Bucher scattering intensity [25] I(s), with the specific expression given by Eq. (4):

$$P(r) = \frac{1}{2\pi^2}\int_0^{\infty} I(s)\, sr\sin(sr)ds \tag{4}$$

The reduced scattering angle $s = 4\pi\sin\theta/\lambda$, and r is the distance from a point to the scattering center.

The pore gyration radius is calculated using the Shull–Roess method [26]. Setting $P(r) = 0$ yields the theoretical maximum pore radius (D_{max}). The pore gyration radius (R_g) is expressed by Eq. (5):

$$R_g = \sqrt{\frac{\int_0^{D_{max}} P(r)r^2 dr}{2\int_0^{D_{max}} P(r)dr}} \tag{5}$$

The length of the pore along the tensile direction is calculated using the Ruland method, expressed by Eq. (6):

$$B_{obs} = \frac{2\pi}{l_c q} + B_{\varphi} \tag{6}$$

where B_{obs} is the half-peak width of the intensity distribution corresponding to the q value in the strip scattering pattern; B_{φ} is the orientation factor of the pore distribution along the tensile direction; l_c represents the length of the oriented pore. Plotting the expression allows estimation of l_c and B_{obs} values from the slope and intercept [27].

3 Results and discussion

Sinoite fibers were subjected to high-temperature treatment in a nitrogen atmosphere to investigate their high-temperature properties and structural evolution. In Fig. 1, fibers treated at room temperature and elevated temperature exhibit smooth surfaces with no obvious defects, showing minimal morphological changes. Fibers treated at 1700 °C display slightly higher surface roughness, although their cross-sections remain relatively smooth and flat. AFM was employed in high-sensitivity mode to scan individual fiber surfaces, characterizing surface roughness changes, as shown in Fig. S2 in the ESM. The surface roughness increased slightly from room temperature to 1600 °C. Elevating the temperature to 1700 °C caused a marked increase in surface roughness, with the most significant changes occurring between 1600 and 1700 °C. The fibers maintained their morphological integrity even under the high-temperature treatment at 1700 °C.

Mechanical properties serve as the core metric for evaluating the application of sinoite fibers. The high-temperature evolution trends of the fiber strength and modulus under different temperature treatments are shown in Fig. 2. At 1400–1600 °C, sinoite fibers exhibit a strength retention rate of 62%–70%. After treatment at 1700 °C, they still maintain a strength of 0.78 GPa, representing a retention rate of 51%. Both the strength and modulus decrease between 1600 and 1700 °C. To systematically evaluate the high-temperature resistance of sinoite fibers, we further investigated their flexibility and high-temperature creep resistance before and after thermal treatment. As shown in Fig. S1 in the ESM, the optical micrographs of fibers after high-temperature treatment reveal no significant changes before and after nitrogen gas treatments. The fibers maintain good luster with no noticeable burrs or fractures. The fiber bundle treated at 1700 °C remained capable of knotting operations. Combined with the SEM image of a single knotted fiber after high-temperature treatment, it can be concluded that sinoite fibers exhibit good flexibility at both room temperature and elevated temperatures.

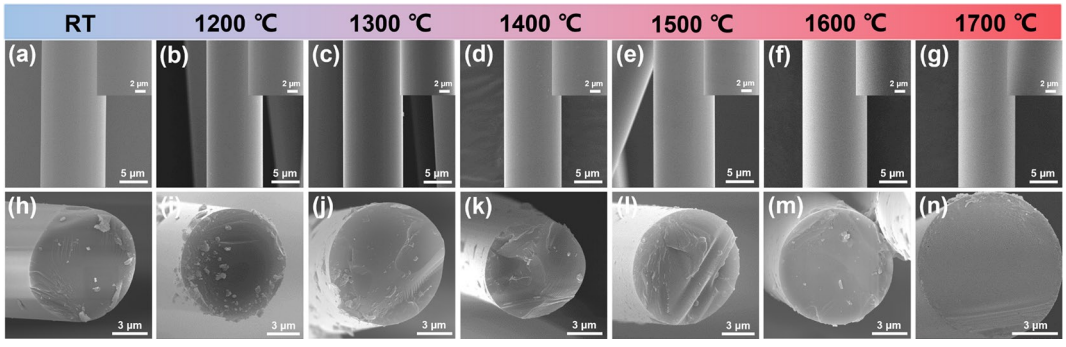

Fig. 1 Scanning electron microscopy morphology of sinoite fibers after nitrogen treatment at room temperature and elevated temperature: (a–g) surface morphology; (h–n) cross-sectional morphology.

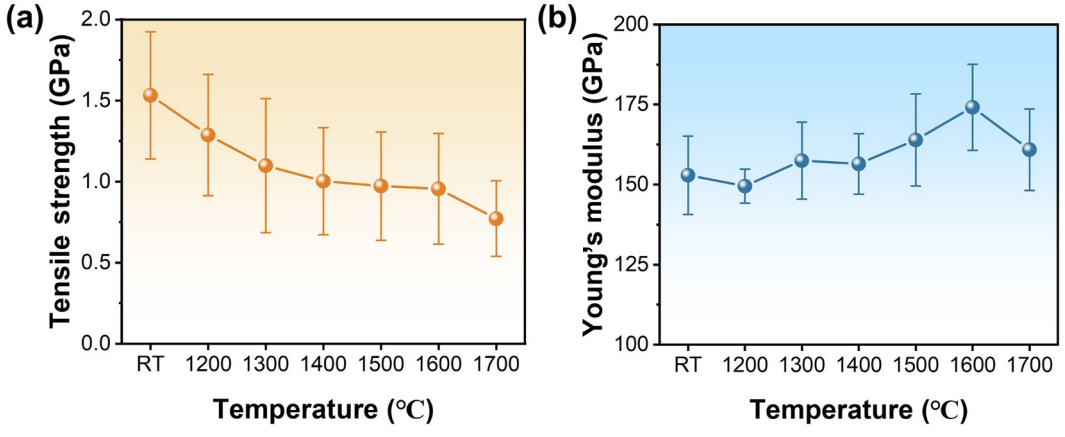

Fig. 2 Evolution of high-temperature mechanical properties of sinoite fibers: (a) tensile strength; (b) Young's modulus.

We employed the bending stress relaxation (BSR) method tailored for ceramic fibers. By measuring the free diameter parameters after high-temperature creep, the stress relaxation ratio (m) can be calculated to evaluate the high-temperature creep resistance of the fibers. As shown in Fig. S3 in the ESM, sinoite fibers were subjected to high-temperature treatment using the fixation method shown. The free diameters of fiber loops at 1500–1700 °C were obtained to calculate the m value. The results indicate that the fibers maintain good high-temperature creep resistance below 1500 °C. As the treatment temperature increases, the high-temperature creep resistance further decreases. These changes in high-temperature performance suggest that structural transformations occur in the sinoite fibers at elevated temperatures.

X-ray characterization techniques are useful for analyzing the reasons for the strength and creep resistance reduction of sinoite fibers within the temperature range of 1600–1700 °C. In Fig. 3, XRD patterns reveal that sinoite fibers maintain an amorphous state from room temperature to 1600 °C, while a distinct crystalline peak for Si_2N_2O is clearly observed at 1700 °C. Further analysis using WAXS 2D patterns revealed symmetrical, uniform, and broadened diffraction rings, indicating that both sinoite fibers treated at room temperature and at 1600 °C exhibit amorphous and isotropic structures. The diffraction rings at room temperature were broader than those at 1600 °C, suggesting a higher degree of disorder [28]. According to PDF Card#79-1539 for the Si_2N_2O phase, fibers treated at 1700 °C exhibit distinct diffraction bands corresponding to the (200) and (111) crystal planes of Si_2N_2O crystallization, matching the high crystalline peaks observed in the XRD pattern [23,29]. Their low orientation indicates that Si_2N_2O grains exhibit no significant alignment along the fiber axis. This suggests that 1600–1700 °C represents the critical temperature range for structural transformation in sinoite fibers, with crystallization at 1700 °C being associated with a decline in mechanical properties.

We employed XPS to characterize the elemental bonding states on the fiber surface and within the fiber, analyzing changes in the chemical structure before and after crystallization treatment at 1600–1700 °C. After profiling at a depth of 400 nm for fibers treated at different temperatures, peak fitting of the XPS spectra yielded the results shown in Fig. 4. In the peak fitting results for room-temperature fibers, the Si 2p peak at 102.4 eV corresponds to O and N single bonds and can be resolved into two peaks: Si–N at 102.3 eV and Si–O at 103.1 eV [30,31]. The N 1s peak at 397.6 eV corresponds to Si, O, and C and can be resolved into a main N–Si peak at 397.5 eV and two shoulder peaks at 399.5 eV (N–C) and 401.8 eV (N–O) [32]. The O 1s peak at 533.0 eV corresponds to different types of O–Si bonds. Since the Si–N bond has a lower binding energy than the Si–O bond, an increase in the number of nitrogen atoms bonded to the silicon tetrahedra reduces the O–Si bond energy. Therefore, it can be further divided into the O–Si bond at 534.5 eV, characteristic of SiO_2, and the O–Si–N bond at the lower energy of 532.5 eV, characteristic of Si_2N_2O [20,23,33].

It is obvious that the chemical bonding patterns of the fibers remain largely unchanged after treatment at 1600–1700 °C, with peak positions showing close assignment while peak intensity undergoes alteration. The peak intensity of O–Si in O 1s, corresponding to SiO_2 (SiO_4 silicon tetrahedra), decreases significantly with increasing treatment temperature. Similarly, the Si–O peak intensity in Si 2p diminishes with increasing temperature. As the temperature increases, O–Si–N becomes the primary structural unit of the silicon tetrahedra. In Fig. S4 in the

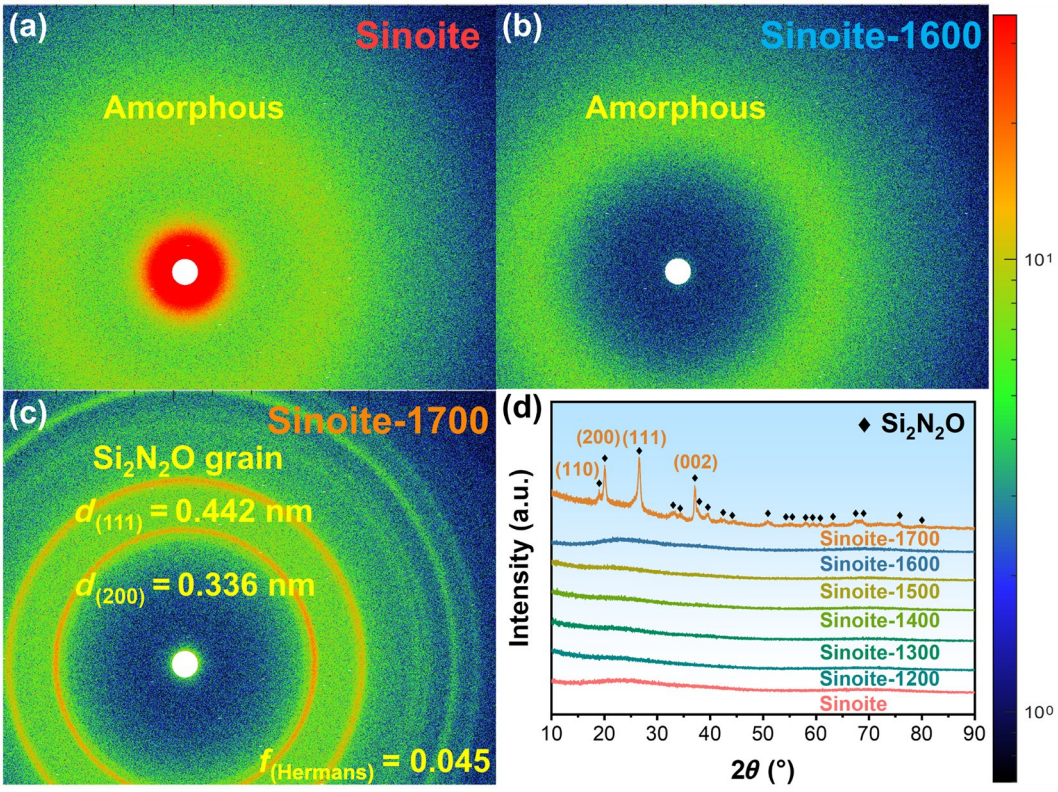

Fig. 3 (a–c) WAXS patterns and (d) XRD patterns of sinoite fibers treated at room temperature and high temperatures.

ESM, the XPS elemental peak fitting diagram of the sinoite fiber surface shows that the variation patterns of Si–O and Si–N bonds in the Si 2p region correspond to the depth profiling results at 400 nm. This indicates that during the transformation of sinoite fibers from an amorphous state to Si_2N_2O crystallization, the structure resembling a SiO_2 network gradually diminishes, while the overall number of nitrogen atoms in silicon tetrahedra increases. Considering that Si_2N_2O crystals form via Si–O–Si bridging from Si_3N_4 silicon tetrahedra, nitrogen-rich silicon tetrahedra are more readily converted into Si_2N_2O crystals at elevated temperatures [34]. In the FT-IR analysis shown in Fig. S5 in the ESM, the absorption peak at 780 cm^{-1} corresponds to symmetric Si–O–Si bonds [35], the peak at 1087 cm^{-1} corresponds to mixed O–Si–N network structures [29], and the peak at 874 cm^{-1} corresponds to asymmetric Si–O–Si bonds [35]. Obviously, nitrogen–oxygen–silicon fibers exhibit minor symmetric Si–O–Si structures at 1600 °C, which transform into more pronounced O–Si–N and asymmetric Si–O–Si structures at 1700 °C. The Si–O–Si structure in SiO_2 crystallization is fully symmetric, whereas asymmetric Si–O–Si and O–Si–N structures suggest the formation of a mixed network of nitrogen-containing silicon tetrahedra bridged by oxygen.

High-temperature treatment significantly influences the transformation of silicon tetrahedral structures with varying nitrogen–oxygen contents in sinoite fibers. To further investigate the transformation patterns of silicon tetrahedra during Si_2N_2O crystallization, we performed peak fitting analysis on ^{29}Si MAS NMR spectra of fibers treated at different temperatures, as shown in Fig. 5. Based on the number of N and O atoms bonded to the Si atom, NMR peaks can be fitted into five distinct structures: SiN_4, SiN_3O, SiN_2O_2, $SiNO_3$, and SiO_4 [36]. Fibers at room temperature exhibit characteristic resonance peaks: a SiN_4 resonance peak at δ = −40 ppm; a SiN_3O resonance peak at δ = −63 ppm [33]; SiN_2O_2 and SiN_3O resonance peaks at δ = −77 ppm and δ = −98 ppm, respectively; and a SiO_4 resonance peak at δ = −118 ppm [22,37]. At this point, two oxygen-rich silicon tetrahedral structures, $SiNO_3$ and SiO_4, constitute the primary structure of room-temperature sinoite fibers. In fibers treated at 1600–1700 °C, the intensity of vibration peaks from nitrogen-rich SiN_3O and SiN_2O_2 tetrahedral structures increases with increasing temperature, while that from $SiNO_3$ and SiO_4 structures gradually decreases; the SiN_3O structure exhibits the strongest vibration peak at 1700 °C. Based on the preceding analysis, as the heat treatment temperature increases, the sinoite fibers gradually transform from symmetrical SiO_4 and high-oxygen-content silicon tetrahedral structures to high-nitrogen-content SiN_3O tetrahedral structures. This transformation leads to the formation of more $N_3Si–O–SiN_3$ structures bridged by oxygen atoms, which arrange themselves into an ordered network to generate Si_2N_2O crystals.

By characterizing the chemical bonding forms and silicon tetrahedral structures of sinoite fibers, we obtained information on their crystalline structural transformations at high temperature. Further investigation into the spatial distribution of these crystalline structures is needed. First, fibers treated at 1600 °C were selected. Using FIB, cross-sections reflecting the radial distribution structure of the fibers were obtained, as shown in Fig. S6 in the ESM. The 1600 °C-treated fibers exhibited a completely amorphous structure, with both surface and inner layers displaying diffraction rings characteristic of amorphous states. Elements were uniformly distributed throughout the fibers, demonstrating structural stability at 1600 °C.

In contrast, the sinoite fibers treated at 1700 °C exhibited a layered structure comprising crystalline Si_2N_2O and amorphous regions, as shown in Fig. 6. In the high-angle annular dark-field (HAADF) images, Si_2N_2O grains on the surface exhibit a tendency for radial inward growth. These elongated columnar grains growing inward combine with amorphous regions to form a

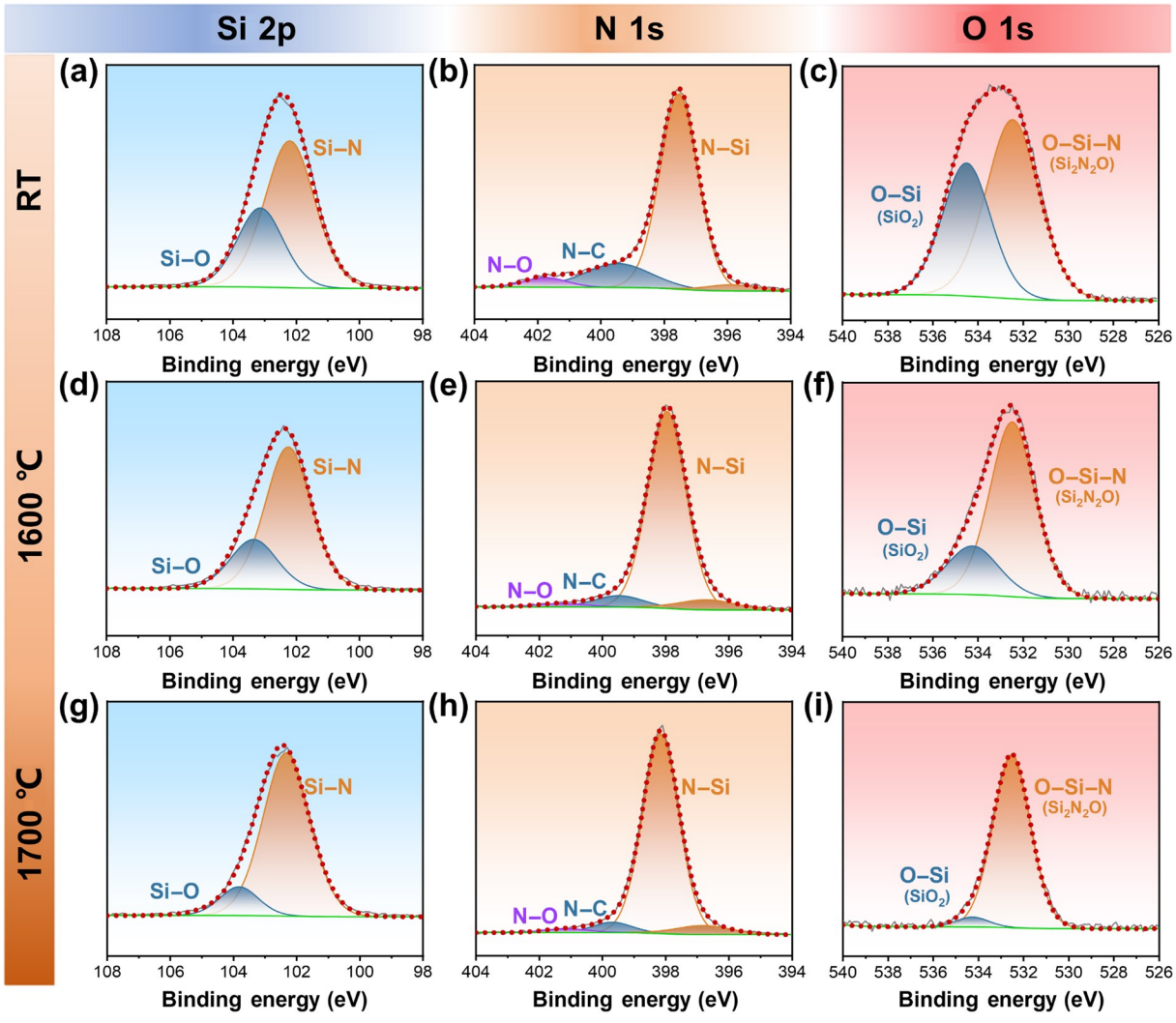

Fig. 4 XPS depth analysis of sinoite fiber elemental peak fitting of Si 2p, N 1s, and O 1s at a depth of 400 nm: (a–c) room temperature; (d–f) 1600 °C; (g–i) 1700°C.

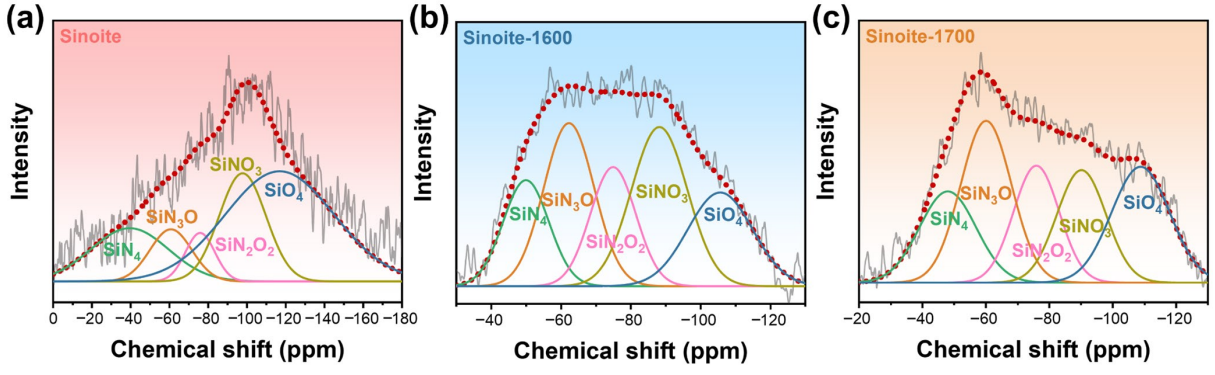

Fig. 5 ^{29}Si MAS NMR peak fitting spectrum of sinoite fibers: (a) room temperature; (b) 1600 °C; (c) 1700 °C.

mosaic-shell structure [38]. This structure is composed of subgrains with minimal orientation differences [39,40]. This explains the presence of minute amorphous regions between sinoite fibers treated at 1700 °C and the associated decrease in strength. Estimated grain sizes from the XRD patterns of 1700 °C-treated fibers are summarized in Table S1 in the ESM, with a high aspect ratio consistent with the formation of prismatic Si_2N_2O grains. Based on PDF Card #79-1539 for the Si_2N_2O phase, lattice fringes corresponding to the Si_2N_2O(200) plane (0.442 nm) and (110) plane (0.466 nm) are observed in the fiber surface region [41,42], consistent with the single-crystal diffraction results from SAED. EDS mapping reveals an uneven distribution of nitrogen and oxygen between the surface Si_2N_2O grains and the interstitial amorphous regions. Specifically, oxygen is concentrated at these interfaces, while nitrogen is less abundant in the boundary areas. This indicates that elemental segregation occurs in the amorphous regions where Si_2N_2O grains contact each other during grain growth.

We further performed FIB sectioning along the fiber axis on sinoite fibers treated at 1700 °C, as shown in Fig. S7 in the ESM. The fibers exhibited surface Si_2N_2O columnar crystals along the axial direction, with an amorphous structure in the inner layer.

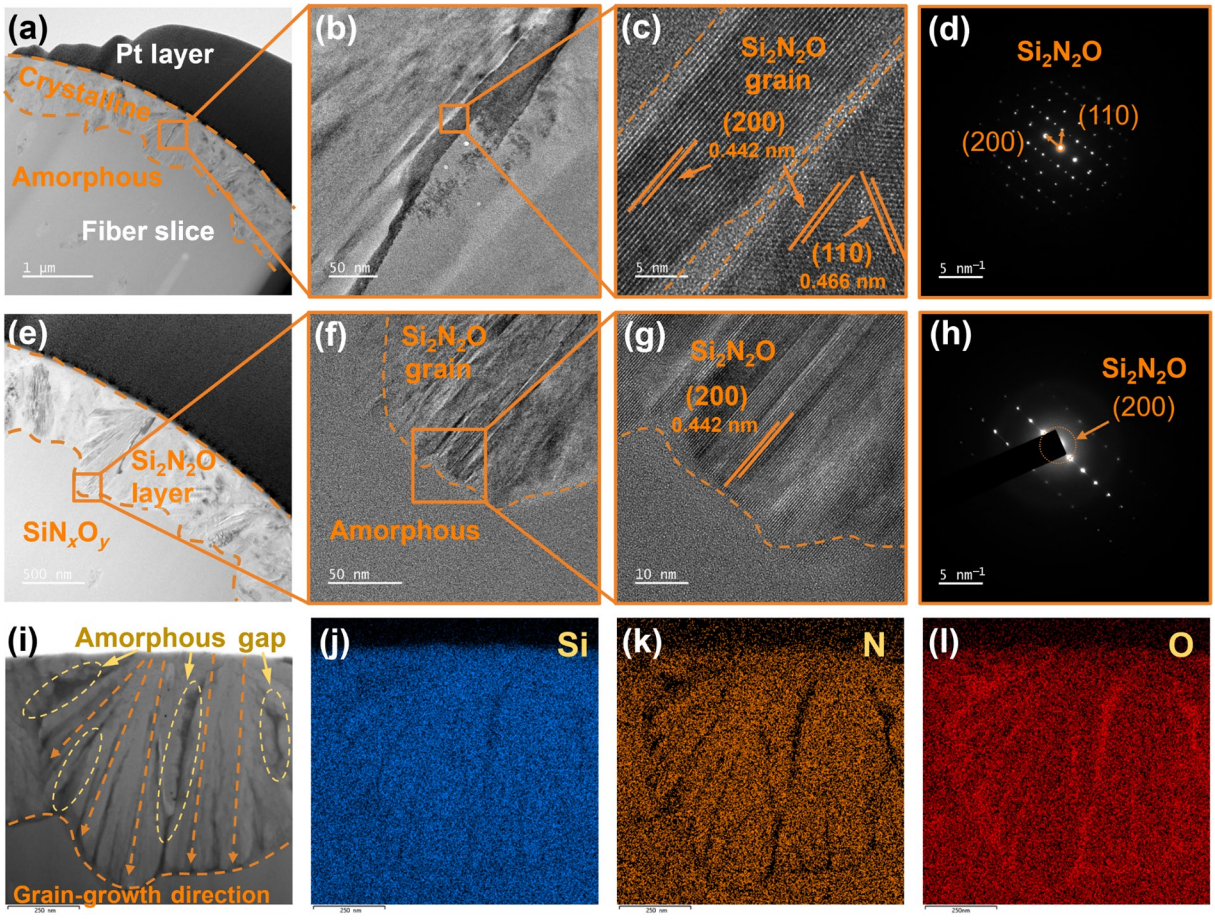

Fig. 6 High-resolution transmission electron microscopy characterization (HR-TEM) of FIB cross-sectioned sinoite fibers treated at 1700 °C: (a–h) HR-TEM images and SAED patterns of different surface regions; (i–l) EDS mapping of various elements in surface regions.

Nitrogen and oxygen element segregation remained observable at the crystalline–amorphous grain boundaries, consistent with the results observed in radial sections of the fibers. Most importantly, the Si_2N_2O columnar grains in the fiber exposed low-index crystal planes in both axial and radial sections. This indicates that Si_2N_2O grains grew spatially along low-index crystal planes with lower energy toward the fiber interior.

We employed aberration-corrected transmission electron microscopy to investigate the surface structure evolution and grain growth mechanisms of sinoite fibers treated at 1700 °C. Analysis of different microdomains within the fibers was conducted using the EELS energy-dispersive spectroscopy module, as shown in Fig. 7. In the dark-field image of the surface layer, a distinct mosaic-shell structure formed by columnar grains can be observed. Furthermore, EELS mapping indicates that the distribution differences of nitrogen and oxygen in the boundary regions are consistent with the EDS results. We selected microarea I, where Si_2N_2O crystallization is denser, and microarea II, a boundary region with less crystallization, to obtain the EELS spectra shown in Fig. S8 in the ESM. By plotting the logarithmic scale, it is obvious to find distinct peaks attributed to the Si–L_3 edge, N–K edge, and O–K edge, enabling the extraction of element-specific EELS spectra. Within the N–K edge, the 401 eV peak corresponds to the near-edge structure of N–Si σ^* [1]. The peak intensity in microarea I is significantly higher than that in microarea II, indicating a greater abundance of N–Si bonds in the crystalline Si_2N_2O region than that in the boundary zone. In the O–K edge, the 532 eV peak corresponds to the symmetric Si–O–Si σ^* oxygen bridge structure [43]. The peak intensity in microarea I is lower, and the peak broadens, indicating that the boundary region contains more regular, symmetric Si–O structures than the Si_2N_2O crystalline region. In the Si–L_3 edge spectrum, 103 eV corresponds to Si–N σ^* and 106 eV corresponds to Si–O σ^* [44]. Microarea I exhibits more Si–N σ^* structures than microarea II, while Si–O σ^* structures are fewer in microarea I than in microarea II, corroborating the N–K and O–K results. The Si–N structure predominates over the Si–O structure in the crystalline Si_2N_2O region, while the Si–O structure is more abundant at the crystalline–amorphous interface. This indicates that during grain growth, silicon tetrahedra in Si_2N_2O grains and the surrounding amorphous regions undergo mutual conversion. Combined with solid-state ^{29}Si NMR spectroscopy results, silicon tetrahedra along the grain growth direction transform from oxygen-rich to SiN_3O structures, forming Si_2N_2O, while excess Si–O structures accumulate at the interface, enriching oxygen in the silicon tetrahedra of the amorphous region.

To investigate the conversion patterns and specific forms of Si–N and Si–O structures during grain growth, we employed TOF-SIMS for etching and surface analysis to obtain the sputtered secondary ion intensity. The sputtered SiN^-, O^-, and Si^- secondary ions enabled quantification of elemental and bonded form contents. The relationship between three-dimensional imaging, surface analysis, and etching secondary ion intensity is shown in Fig. 8. The combined three-dimensional ion distribution on the fiber surface and interior reveals that with increasing temperature, the overall intensity of SiN^- increases, while that of O^- decreases. The 1700 °C-treated fibers exhibit enhanced SiN^- and Si^- intensities, gradually approaching the stoichiometric ratio of

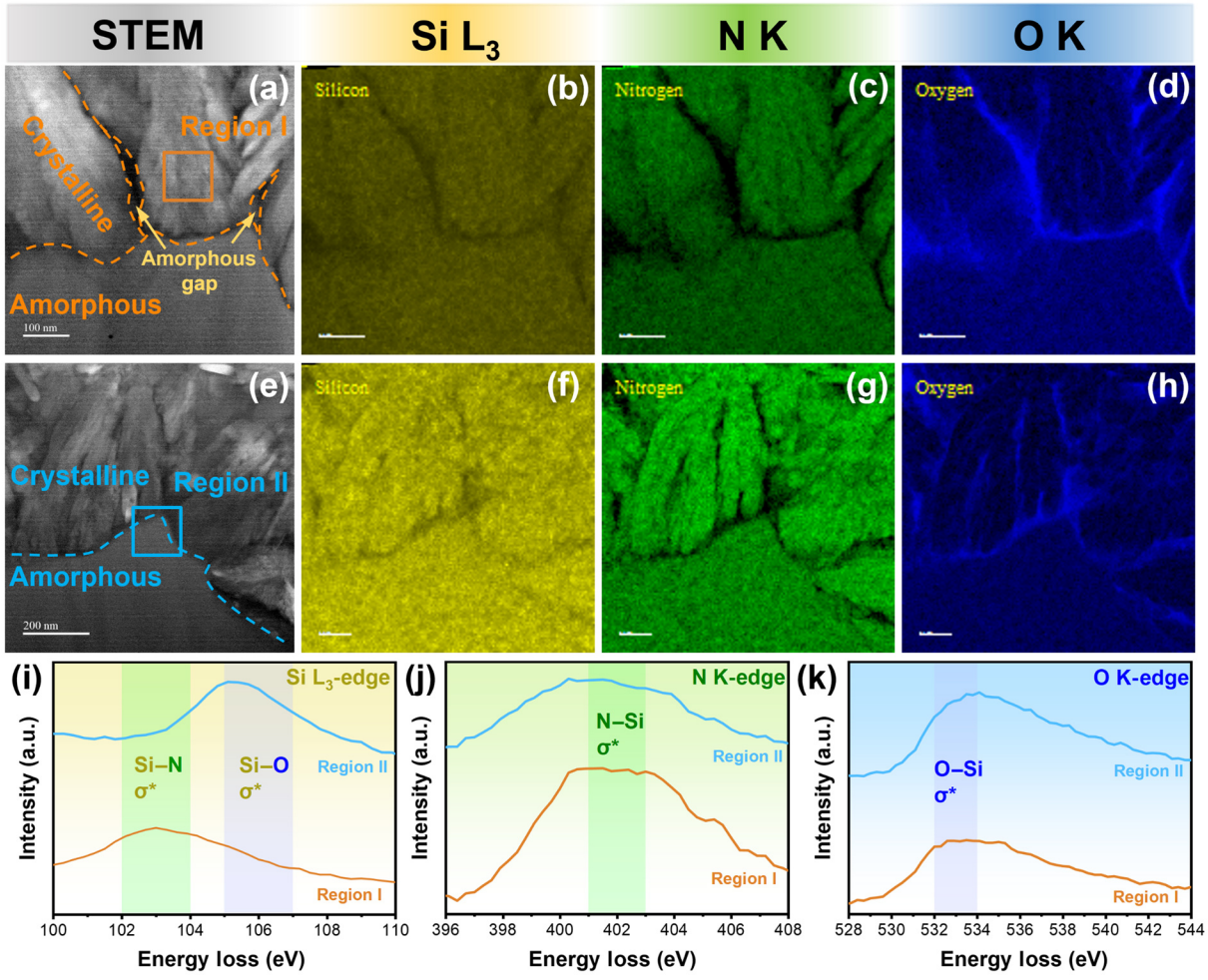

Fig. 7 Dual-aberration-corrected high-resolution transmission electron microscopy characterization of FIB-sectioned sinoite fibers treated at 1700 °C: (a–h) EELS mapping of different surface regions; (i–k) EELS spectra and bonding configurations at Si–L_3, N–K, and O–K edges for microareas I in (a) and II in (e).

Si_2N_2O. Combined with the preceding TEM and EELS analyses, the growth of Si_2N_2O grains requires N and O element segregation into the surrounding amorphous regions, thereby forming more Si–N structures and increasing the Si–O structures within the amorphous regions.

Sinoite fibers demonstrate thermodynamically stable Si_2N_2O crystals above 1700 °C, endowing them with exceptional high-temperature resistance. Theoretically, the closer the stoichiometric ratio of amorphous silicon oxynitride approaches that of Si_2N_2O, the easier it is to form Si_2N_2O crystals at high temperature, resulting in a more stable structure that enhances high-temperature performance [41]. The relative nitrogen–oxygen content in sinoite fibers also significantly influences Si_2N_2O crystallization and high-temperature resistance. Therefore, we simulate the energy and structural changes of sinoite fibers during heating to 1700 °C by using first-principles calculations based on density functional theory. The specific process is detailed in the ESM. Figure S9 in the ESM shows a series of structural fragments obtained from a randomly generated silicon oxynitride system with varying Si, N, and O atom ratios during heating from 0 to 1700 °C within 0–60 ps. During this process, we captured the evolution of SiN_3O tetrahedral structures within the fragments over time in Fig. S10 in the ESM. As the temperature increases, SiN_3O structures progressively proliferate within the four distinct silicon oxynitride systems. The Si_2N_2Osystem with ideal atomic ratios exhibits the highest SiN_3O network density at 1700 °C. The developed sinoite fibers ($Si_{1.82}N_{2.16}O$) closely approximate the Si_2N_2O composition in stoichiometry. Therefore, in the sinoite fibers we developed, the number of SiN_3O tetrahedral structures is second only to that in Si_2N_2O, which has an ideal atomic ratio. Conversely, silicon oxynitride systems with appropriately increased O and N contents exhibit fewer SiN_3O tetrahedra, indicating that the initial elemental composition of sinoite fibers determines the level of difficulty in forming Si_2N_2O crystals.

The root-mean-square displacement (RMSD), total energy, and radial distribution function (RDF) serve as core metrics for evaluating the stability and internal bonding patterns of different systems, as illustrated in Fig. 9. The RMSD values primarily reflect the intensity of structural changes during heating. The values for all four systems indicate moderate structural alterations, gradually stabilizing toward the end of the heating process. This suggests the gradual conclusion of the structural transformation process, forming the foundation for the accuracy of simulation results [45]. Among these, the Si_2N_2O system with an ideal atomic ratio exhibits the least structural change, followed by the developed sinoite fibers. The trends in total energy changes across the four systems also align with the RMSD patterns, indicating that the sinoite system near the Si_2N_2O atomic ratio demonstrates superior thermodynamic stability. The radial distribution function reflects the probability distribution of different structures across chemical bond lengths. As the bond length increases, the probability distribution gradually stabilizes through a series of transitions. The first peak typically corresponds to short, strong covalent bonds within the system, with Si–O and Si–N bond lengths typically

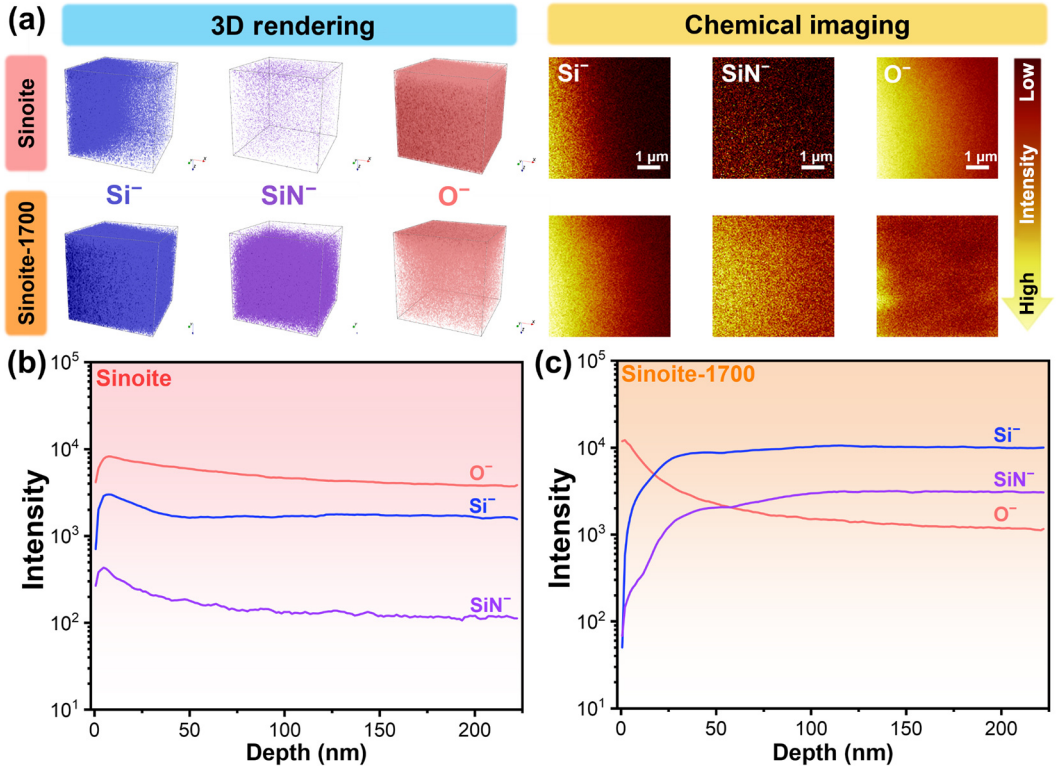

Fig. 8 Secondary ion distribution obtained by TOF-SIMS for sinoite fibers treated at room temperature and 1700 °C: (a) three-dimensional ion distribution imaging and surface analysis; (b, c) distribution of secondary ion signals versus depth at room temperature and 1700 °C.

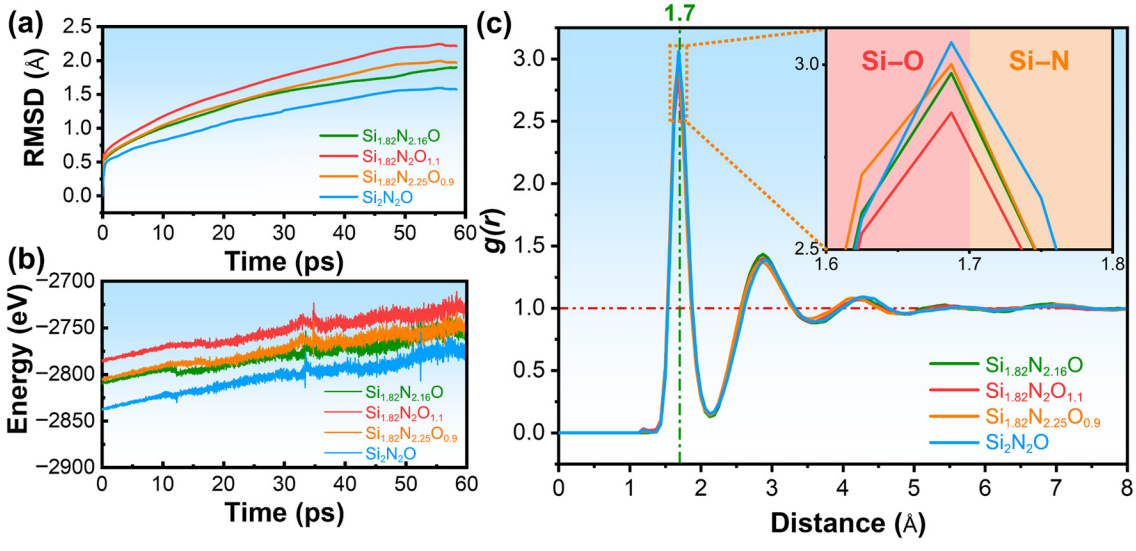

Fig. 9 Core metrics of four systems: sinoite fiber ($Si_{1.82}N_{2.16}O$), ideal atomic ratio (Si_2N_2O), high-nitrogen ($Si_{1.82}N_{2.25}O_{0.9}$), and high-oxygen ($Si_{1.82}N_2O_{1.1}$) systems based on first-principles calculations: (a) root-mean-square displacement; (b) total energy change; (c) radial distribution function.

ranging between 1.6–1.7 and 1.7–1.8 Å, respectively [45]. The peak position indicates the highest distribution probability for Si–O and Si–N bonds among the four systems. An enlarged view of the peak reveals differences in the probability distribution of Si–O and Si–N bonds across systems. The Si_2N_2O system with ideal atomic ratios exhibits the highest Si–N distribution probability. The developed sinoite fibers show moderate distribution probabilities for both chemical bonds, while the two systems with different N&O contents display significantly different bonding probability distributions compared with the previous system. The combined results of these simulations demonstrate that the sinoite fiber close to the Si_2N_2O composition is fundamental to its structural stability. At elevated temperature, this composition facilitates the formation of a more extensive SiN_3O tetrahedral network, thereby promoting the crystallization of the Si_2N_2O phase. Based on the calculated thermal stability of the fibers, we measured their TG–DSC curves, as shown in Fig. S11 in the ESM. The fibers exhibited no weight loss and no endothermic peaks below 1500 °C, confirming the excellent high-temperature thermal stability of the sinoite fibers.

Defects in sinoite fibers typically manifest as nanoscale pores, making them difficult to observe through morphological characterization methods. Consequently, no distinct pores were observed in either the SEM or TEM images. To analyze the

evolution of pores in sinoite fibers before and after 1700 °C treatment, small-angle X-ray scattering (SAXS) was employed to characterize the pore size distribution and orientation within the fibers. The 2D SAXS patterns and pore-related parameters of sinoite fibers are shown in Fig. 10. The 2D images were processed using Fid 2D software and corrected for silver behenate standard and air background samples. Different colors in the figure represent varying levels of scattering intensity. Fibers treated at 1600–1700°C exhibited an overall higher scattering intensity than at room-temperature samples, indicating pore expansion with increasing temperature. Additionally, fibers at different temperatures showed higher equatorial scattering intensity than meridional intensity, suggesting a degree of orientation of pores along their normal direction (radially along the fiber) [26,27]. We selected a sector covering the equatorial direction from the 2D SAXS pattern for azimuthal integration, obtaining the relationship between scattering intensity and scattering vector. Since the scattering vector is inversely proportional to pore size, the distribution of larger pores in high-temperature-treated sinoite fibers exceeds that of room-temperature fibers. Furthermore, using the Shull–Roess method, we calculated the pore size distribution curve and the radius of gyration for the sinoite fibers. We found that even after high-temperature treatment, the maximum porosity of the fibers was less than 0.17%. The radius of gyration indicates the average size of existing pores, and it increases slightly with increasing treatment temperature [26]. Using the Ruland method, we fitted a curve for the half-peak width of the intensity distribution at a specific scattering vector. Based on the fitted-curve equation, the slope and intercept allowed us to estimate the average pore length and orientation degree along the orientation direction. Fibers treated at higher temperatures exhibited a greater orientation degree and larger average pores than at room-temperature fibers, while those treated at 1700 °C showed a slightly lower orientation degree than those treated at 1600 °C. Considering that pore orientation is primarily along the diameter direction, this may be attributed to the presence of dislocations featuring a mosaic-shell structure, which partially eliminates defects and thereby reduces pore orientation.

Based on the "dissolution–precipitation" mechanism, the formation of liquid or molten phases can dissolve multiple solid phases, thereby overcoming the limitations of solid–solid interfaces and significantly enhancing mass transfer and reaction rates [20,46,47]. TEM observations reveal significant oxygen enrichment along the grain growth direction within the Si_2N_2O mosaic shell. (Figs. 6 and 7). Furthermore, XPS surface analysis (Fig. S4 in the ESM) indicates abundant surface Si–O bonds at all temperatures. This confirms the presence of molten SiO_2 on the fiber surface at 1700 °C, which solidifies into a glassy state upon cooling. We therefore tentatively propose that the nucleation and grain growth of Si_2N_2O occur within a liquid SiO_2 phase. At high temperature, molten SiO_2 serves both as an elementally segregated product forming a Si_2N_2O core and as a liquid-phase medium for Si_2N_2O grain growth. The formation of a liquid-phase SiO_2 at grain boundaries significantly accelerates material exchange and reaction rates, facilitating dissolution of materials at grain boundaries and rearrangement of silicon tetrahedra, thereby increasing the reaction rate by an order of magnitude. The reduced surface energy at material interfaces facilitates heterogeneous nucleation at these boundaries. This explains why Si_2N_2O grains with mosaic-shell structures are distributed only on the fiber surface layer, while the inner layer remains amorphous [48]. Previous studies have reported that certain partial pressures of the external atmosphere (N_2, H_2, CH_4, etc.) significantly influence grain nucleation and growth rates at contact interfaces. Elevated nitrogen partial pressure promotes nucleation and growth of diamond films along the (111) planes [48]. Other researchers found that increased external nitrogen partial pressure reduces the nucleation radius and grain growth activity, thereby enhancing the nucleation rate [49]. Analysis of the fiber cross-sectional morphology after 1700 °C nitrogen treatment indicates that radially distributed Si_2N_2O grains on the fiber surface form via heterogeneous nucleation. This mechanism arises from the low gas–solid surface energy between nitrogen gas and sinoite fibers at

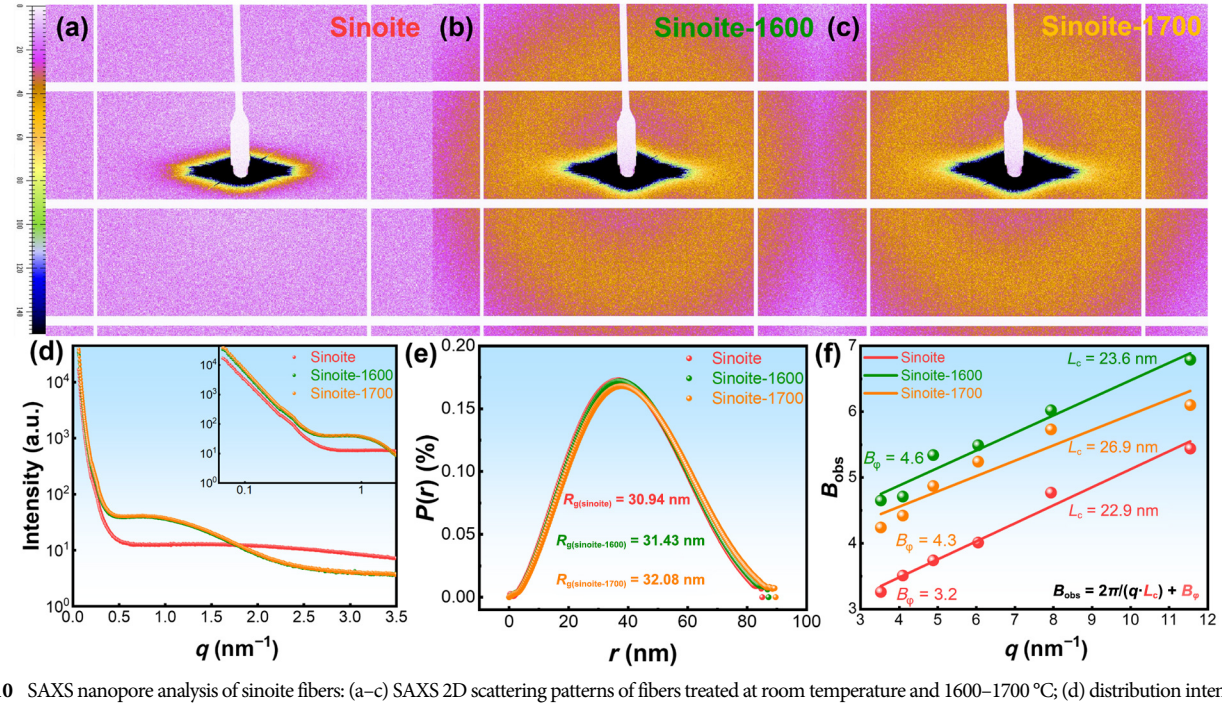

Fig. 10 SAXS nanopore analysis of sinoite fibers: (a–c) SAXS 2D scattering patterns of fibers treated at room temperature and 1600–1700 °C; (d) distribution intensity of pore scattering vectors; (e) average porosity distribution and pore radius of gyration for different nanopore sizes; (f) pore length and orientation factor along pore orientation.

high temperature, which promotes nucleation on the fiber surface. Grain growth then proceeds via the SiO_2 liquid phase.

In previous research, researchers have elucidated the mechanisms of heterogeneous nucleation on ceramic surfaces in high-temperature environments or the formation of liquid phases via liquid-phase sintering of silicon powder. This is crucial for understanding the intrinsic mechanism of nucleation and grain growth of Si_2N_2O in sinoite fibers, which forms the mosaic-shell structure [47–49]. As shown in Fig. 11, the process can be broadly categorized by treatment temperature into three processes: heating to 1600 °C at room temperature, reaching 1700 °C, and preserving at 1700 °C for 1 h. As the temperature increases, the other silicon tetrahedra in $Si_xN_yO_z$ gradually undergo a rearrangement, transforming into SiN_3O. Specifically, fibers treated at 1600–1700°C undergo more intricate transformations: I. The amorphous $Si_xN_yO_z$ phase can be considered to have the form $(Si_3N_4)_a(SiO_2)_b(Si_2N_2O)_c$. As the temperature increases, the rearrangement of silicon tetrahedra leads to separation into $(SiO_2)_b$ and $(Si_2N_2O)_c$ structures. Based on the initial stoichiometry of the sinoite fiber, we can calculate a form of approximately $(Si_3N_4)_{0.4}(SiO_2)_{0.42}(Si_2N_2O)_{0.28}$. As a result of elemental segregation, trace amounts of the $(SiO_2)_b$ structure remained. Concurrently, the contact surface between the nitrogen atmosphere and the fiber under high-temperature treatment exhibits low surface energy. II. At 1700 °C, amorphous SiO_2 on the fiber surface melts to form an oxygen-rich liquid phase layer. Si–O and Si–N networks come into full contact and rearrangement, and heterogeneous nucleation preferentially occurs at low-surface-energy interfaces, forming Si_2N_2O crystal nuclei. III. Continuous heating at 1700 °C enables grains with the orientation most favorable for radial growth to persistently grow along low-index crystal planes within the liquid phase. Due to the asynchrony between nucleation and growth rates, columnar Si_2N_2O grains with a mosaic structure form along the growth direction as the vitreous SiO_2 cools. Ultimately, through these processes, the radial arrangement of Si_2N_2O columnar crystals formed a mosaic-shell layer, while the fiber surface layer exhibited an amorphous oxygen-rich zone.

After analyzing the crystallization mechanism of the surface layer of sinoite fibers, we discuss the coupling mechanism between the series of microstructural evolutions and the mechanical properties of sinoite fibers:

(i) Grain overgrowth: Sinoite fibers maintain a compositionally uniform amorphous structure without long-range ordered grain structures from room temperature to 1600 °C. Crystallization at 1700 °C triggers phase separation and crystallization of Si_2N_2O. The low nucleation rate and high growth rate associated with heterogeneous surface nucleation cause Si_2N_2O grains to grow abnormally large along low-index crystal planes into the fiber interior. These grains form brittle grain boundaries with the amorphous matrix, becoming the primary source of cracks.

(ii) Microdefect evolution: Based on SAXS pore analysis, atomic-scale coordination defects and microvoids serve as defect sources in fibers from room temperature to 1600 °C. As the temperature increases, a slight rise in microdefects causes a gradual decrease in tensile strength. Above 1700 °C, Si_2N_2O grains excessively grown via the glassy SiO_2 liquid phase, along with brittle grain boundaries with the surrounding amorphous matrix, become the primary defect sources. Although the orientation of microvoids along the fiber diameter decreases, the average microdefect size continues to increase, leading to further strength reduction. The Young's modulus of crystallized fibers also decreases due to the amplification of surface and internal defects and the formation of brittle grain boundaries.

Figure 12 summarizes studies on the high-temperature performance evolution of various nitride and oxide fibers in a nitrogen atmosphere [6,7,9,11,12], demonstrating the superior temperature resistance of sinoite fibers. Although some studies report higher initial strengths for silicon nitride fibers than for our sinoite fibers, their strengths approach those of sinoite fibers between 1200 and 1400 °C. However, sinoite fibers demonstrate significantly superior high-temperature performance compared with common nitride and oxide fibers above 1500 °C. In the radar chart, our novel sinoite fibers exhibit small diameters, light weight with high strength, and outstanding temperature resistance. Its

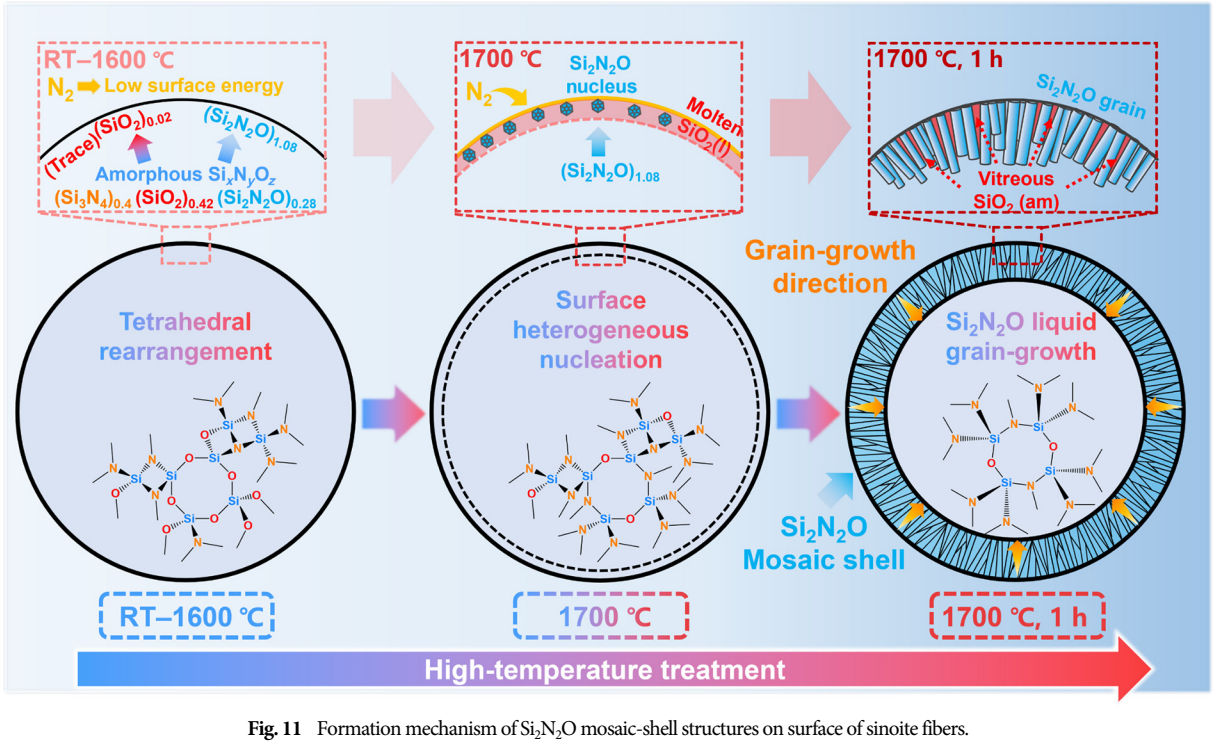

Fig. 11 Formation mechanism of Si_2N_2O mosaic-shell structures on surface of sinoite fibers.

清華大学出版社 Tsinghua University Press | SciOpen

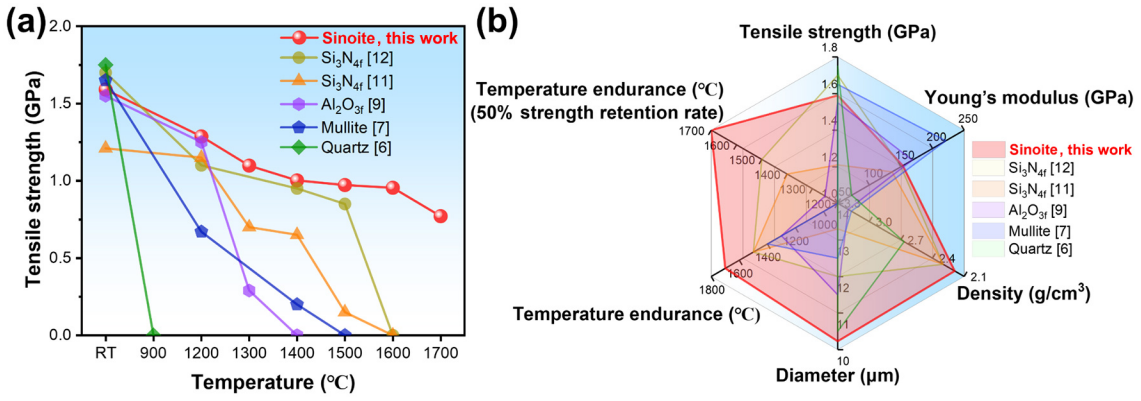

Fig. 12 Comparison of high-temperature resistance between sinoite fibers and other low-dielectric ceramic fibers under high-temperature treatment.

maximum temperature tolerance at the half-strength retention rate far exceeds that of other fibers. This stems from the near-stoichiometric Si_2N_2O ratio, which maintains the amorphous state of the fibers below 1700 °C. The low energy of the Si_2N_2O phase formed at high temperature allows the fibers to retain their strength even beyond 1700 °C.

4 Conclusions

In this work, we developed a near-stoichiometric continuous sinoite fiber resistant to 1700 °C. We investigated its compositional structure and performance evolution along with the high-temperature mosaic-shell formation mechanism. The reported sinoite fibers exhibit a tensile strength of 1.53 GPa at room temperature and low-dielectric properties, which maintain an amorphous state and structural stability below 1600 °C, retaining 51% of the strength at 1700 °C. The extremely low internal porosity ensures the strength retention ratio after high-temperature treatment. At 1700 °C, Si_2N_2O grains with a radially distributed, mosaic-shell structure form on the surface of sinoite fibers. This process follows the mechanism of heterogeneous nucleation at the surface and dissolution-growth in an oxygen-rich SiO_2 liquid phase. Essentially, it involves the tetrahedral rearrangement of Si–N and Si–O bond networks and the elemental segregation between the crystalline grains and the amorphous regions along the grain-growth direction. First-principles calculations based on density functional theory indicate that near-stoichiometric sinoite fibers facilitate the formation of more bond networks, thereby promoting Si_2N_2O phase formation and exhibiting superior thermodynamic stability. Compared with regular dielectric ceramic fibers, the novel sinoite fibers maintain a high strength retention rate at temperatures ranging from 1500 to 1700 °C, demonstrating significant high-temperature performance advantages. This lays the foundation for their application in high-temperature structural-functional integrated composites.

Acknowledgements

This work was financially supported by the Advanced Materials-National Science and Technology Major Project (No. 2025ZD0613500), National Natural Science Foundation of China (Nos. 52572038 and 52572090), and the Science and Technology Innovation Program of Hunan Province (No. 2025RC1046).

Author contributions

Zhiqian Liu: responsible for design, experiments, data processing and analysis, and manuscript writing. Xin Long: writing – review and editing, supervision, funding acquisition. Qiansi Zhang: experimental preparation and research. Zhangbocheng Tang: inspection and proofreading. Bing Wang: writing – review and editing, supervision, funding acquisition, methodology, conceptualization. Changwei Shao: writing – review and editing, supervision, resources, funding acquisition, methodology, conceptualization.

Availability of data and materials

The data that support the findings of this study are available from the corresponding author upon reasonable request.

Competing interests

The authors have no competing interests to declare that are relevant to the content of this article.

Electronic Supplementary Material

Supplementary material is available in the online version of this article at https://doi.org/10.26599/JAC.2026.9221265.

References

[1] Long X, Wu ZY, Shao CW, *et al.* High-temperature oxidation behavior of SiBN fibers in air. *J Adv Ceram* 2021, **10**: 768–777.

[2] Nag A, Rao RR, Panda PK. High temperature ceramic radomes (HTCR)—A review. *Ceram Int* 2021, **47**: 20793–20806.

[3] Zhang YP, Tian ZL, Zheng LY, *et al.* Effects of BN coating on the oxidation and crystallization behavior of Si_3N_4 fibers. *Corros Sci* 2024, **240**: 112434.

[4] Hu X, Shao CW, Wang J, *et al.* Characterization and high-temperature degradation mechanism of continuous silicon nitride fibers. *J Mater Sci* 2017, **52**: 7555–7566.

[5] Bocanegra-Bernal MH, Matovic B. Mechanical properties of silicon nitride-based ceramics and its use in structural applications at high temperatures. *Mat Sci Eng A—Struct* 2010, **527**: 1314–1338.

[6] Zhang X, Xiao B, Hou YZ, *et al.* Mechanical properties and microstructure of quartz fiber-reinforced silica matrix composite with a single layer pyrocarbon interphase. *Ceram Int* 2024, **50**: 54566–54574.

[7] Almeida RSM, Tushtev K, Clauß B, *et al.* Tensile and creep performance of a novel mullite fiber at high temperatures. *Compos Part A—Appl S* 2015, **76**: 37–43.

[8] Cooke TF. Inorganic fibers—A literature review. *J Am Ceram Soc* 1991, **74**: 2959–2978.

[9] Li WX, Ji XY, Gai K, *et al.* Regulating crystalline behavior to create fully crystallized α-Al_2O_3-mullite continuous ceramic fibers derived from the melt-spinning of polymer precursor. *Ceram Int* 2025, **51**: 7897–7905.

[10] Sun X, Liu HT, Yang LW, *et al.* Fracture toughness of Si_3N_4 fibers: A combined methodology based on single-edge notch tension and micropillar splitting. *Ceram Int* 2018, **44**: 22036–22040.

[11] Hou YB, Li B, Shao CW, *et al.* Effect of high-temperature annealing in air and N_2 atmosphere on the mechanical properties of Si_3N_4 fibers. *Mat Sci Eng A—Struct* 2018, **724**: 502–508.
[12] Zhang J, Zhang JY, Mei SY, *et al.* Degradation behavior of amorphous silicon nitride fibers in low atmospheric pressure. *J Mater Sci* 2021, **56**: 13964–13974.
[13] Sekine M, Katayama S, Mitomo M. Preparation of silicon oxynitride glass fibers by ammonolysis of silica gels. *J Non-Cryst Solids* 1991, **134**: 199–207.
[14] Okamura K, Sato M, Hasegawa Y. Silicon nitride fibers and silicon oxynitride fibers obtained by the nitridation of polycarbosilane. *Ceram Int* 1987, **13**: 55–61.
[15] Chollon G, Vogt U, Berroth K. Processing and characterization of an amorphous Si–N–(O) fibre. *J Mater Sci* 1998, **33**: 1529–1540.
[16] Zheng YH, Liu Y, Liu RX, *et al.* Preparation of porous Si_3N_4 ceramics with excellent mechanical properties: Effect of the grain growth mechanism on microstructure evolution. *Ceram Int* 2025, **51**: 798–804.
[17] Liu B, Wang JY, Li FZ, *et al.* Effect of interstitial lithium atom on crystal and electronic structure of silicon oxynitride. *J Mater Sci* 2009, **44**: 6416–6422.
[18] Fruhstorfer J, Kerber F, Weigelt C, *et al.* Activated reaction synthesis of silicon oxynitride from silica and silicon nitride. *Ceram Int* 2018, **44**: 8467–8475.
[19] Yin CF, Chen JJ, Yang JR, *et al.* Thermo–mechanical behavior of light spinel-based composites with *in situ* synthesis of Si_2N_2O–SiC. *Ceram Int* 2025, **51**: 14337–14345.
[20] Zhang XW, Wang QH, Yang SW, *et al.* Novel coated Si_2N_2O/SiO_2 crucible for photovoltaic Si growth: Crystallization behavior and interaction with molten Si. *Ceram Int* 2024, **50**: 50107–50117.
[21] Lin SJ, Ye F, Ma J, *et al.* Fabrication of multilayer electronic magnetic window material by Si_2N_2O decomposition. *Mater Design* 2016, **97**: 51–55.
[22] Wen JB, Wang HJ, Fan L, *et al.* Non-additive sintering of Si_2N_2O ceramic with enhanced high-temperature strength, oxidation resistance, and dielectric properties. *Ceram Int* 2021, **47**: 25689–25695.
[23] Jin X, Sun Y, Zhao L, *et al.* Reactive spark plasma sintering of Si_2N_2O ceramic: Reaction process, microstructure, mechanical and dielectric properties. *Ceram Int* 2024, **50**: 12802–12809.
[24] Wang CY, Long X, Shao CW, *et al.* Synthesis of liquid polysilazoxanes for Si–O–C–N ceramics with adjustable composition and high-temperature properties. *Appl Organomet Chem* 2025, **39**: e70253.
[25] Nasiri S, Rabiei M, Palevicius A, *et al.* Modified Scherrer equation to calculate crystal size by XRD with high accuracy, examples Fe_2O_3, TiO_2 and V_2O_5. *Nano Tr* 2023, **3**: 100015.
[26] Xing SZ, Wang GS, Guo HH, *et al.* Synchrotron radiation SAXS and WAXS study of microstructural evolution during graphitization of rayon-based carbon fibers. *J Alloy Compd* 2025, **1035**: 181511.
[27] Liu T, Han C, Wang SS, *et al.* Embedding thermostable rGO/SiC_xO_y composite phase in SiC fibers for improved high temperature resistance. *Carbon* 2025, **233**: 119858.
[28] Zhang YB, Wang B, Meng FX, *et al.* Influence of micro-tension on fiber orientation and crystallization in continuous polymer-derived boron nitride fiber. *Ceram Int* 2024, **50**: 3270–3275.
[29] Liu J, Wang QH, Li YW, *et al.* Inhibiting crystallization of fused silica ceramic at high temperature with addition of α-Si_3N_4. *Ceram Int* 2021, **47**: 11394–11404.
[30] Li YH, Wu HD, Chen XZ, *et al.* Vat photopolymerization of complex-shaped silicon nitride ceramics with high mechanical and thermal performance by optimization sintering aids and kinetics. *J Eur Ceram Soc* 2025, **45**: 117014.
[31] Gong ZY, Xu ZK, Zhang J, *et al.* The microstructure and mechanical properties of Si_3N_{4f}/BN/SiBCN microcomposites fabricated by the PIP process. *Materials* 2024, **17**: 2457.
[32] Takahashi M, Mizokuro T, Nishioka Y, *et al.* Experimental and theoretical studies on N 1s levels of silicon oxynitride films. *Surf Sci* 2002, **518**: 72–80.
[33] Hu X, Shao CW, Wang J, *et al.* Effects of residual radicals on compositional and structural stability of silicon nitride fibers. *J Eur Ceram Soc* 2017, **37**: 4497–4503.
[34] Liu B, Wang JY, Li FZ, *et al.* Atomic-scale studies of native point defect and nonstoichiometry in silicon oxynitride. *J Phys Chem Solids* 2009, **70**: 982–988.
[35] Luan Q, Wang YS, Wang Y, *et al.* The antioxidative protection mechanism of the ultra-high temperature radome composite material BN_f/SiBN. *Ceram Int* 2024, **50**: 36588–36595.
[36] Lipowitz J. Structure and properties of ceramic fibers prepared from organosilicon polymers. *J Inorg Organomet P* 1991, **1**: 277–297.
[37] Hu JB, Zhang B, Li C, *et al.* Fabrication of Si_3N_4 ceramics with high thermal conductivity and flexural strength via novel two-step gas-pressure sintering. *J Eur Ceram Soc* 2022, **42**: 4846–4854.
[38] Shu GY, Dai B, Ralchenko VG, *et al.* Epitaxial growth of mosaic diamond: Mapping of stress and defects in crystal junction with a confocal Raman spectroscopy. *J Cryst Growth* 2017, **463**: 19–26.
[39] Li K, Zhang J, Mo PC, *et al.* Optimizing single crystal diamond mosaic growth: A study on seed thickness variation and pre-growth treatment. *J Cryst Growth* 2025, **649**: 127953.
[40] Wang HX, Wang YF, Liang X, *et al.* Dislocation engineering: Unlocking functional potential in ceramics. *J Eur Ceram Soc* 2026, **46**: 117918.
[41] Geng YQ, Zhao YX, Yue F, *et al.* A novel method to synthesize pure-phase Si_2N_2O powders in a fluidized bed reactor. *Ceram Int* 2022, **48**: 33066–33071.
[42] Luo JT, Luo SY, Gu YF, *et al.* Quantitative analysis of toughening effect of crack deflection on Si_3N_4/Si_2N_2O composites through improved indentation method. *Ceram Int* 2018, **44**: 1894–1901.
[43] Skiff WM, Carpenter RW, Lin SH, *et al.* K, L, M, N, O and P ionization cross-sections for electron energy loss spectroscopy. *Ultramicroscopy* 1988, **25**: 47–60.
[44] Wang D, Penner S, Su DS, *et al.* Silicide formation on a Pt/SiO_2 model catalyst studied by TEM, EELS, and EDXS. *J Catal* 2003, **219**: 434–441.
[45] Jafari H, Ameri E, Soltanolkottabi F, *et al.* Three new reduced forms of synthesized Schiff bases as potent anti-corrosion inhibitors for carbon steel in artificial seawater. *J Mater Sci—Mater En* 2024, **19**: 33.
[46] Hamdi H, Abedi HR, Zhang Y. A review study on thermal stability of high entropy alloys: Normal/abnormal resistance of grain growth. *J Alloy Compd* 2023, **960**: 170826.
[47] Zhang GT, Zheng Y, Zhang JJ, *et al.* Growth of ceramic grains during liquid-phase sintering in Ti(C,N)-based cermets prepared by *in situ* carbothermal reduction of TiO_2. *Int J Refract Met H* 2019, **85**: 105060.
[48] Nakano Y, Zhang XF, Kobayashi K, *et al.* Impact of nitrogen doping on homoepitaxial diamond (111) growth. *Diam Relat Mater* 2022, **125**: 108997.
[49] He PW, Liu ED, Li ZJ, *et al.* Study on the staged precipitation behavior of nitrogen in pure iron during the GASAR zone melting process. *Appl Surf Sci* 2025, **705**: 163552.